# Super-resolution imaging for sub-IR frequencies based on total internal reflection

Lauren E. Barr,[1],*,[†] Peter Karlsen,[1],[†] Samuel M. Hornett,[1] Ian R. Hooper,[1] Michal Mrnka,[1] Christopher R. Lawrence,[2] David B. Phillips,[1] and Euan Hendry[1]

[1]*Department of Physics and Astronomy, University of Exeter, Exeter, EX4 4QL, UK*
[2]*QinetiQ, Cody Technology Park, Ively Road, Farnborough, GU14 0LX, UK*
*Corresponding author: l.barr@exeter.ac.uk*

For measurements designed to accurately determine layer thickness, there is a natural trade-off between sensitivity to optical thickness and lateral resolution due to the angular ray distribution required for a focused beam. We demonstrate a near-field imaging approach that enables subwavelength lateral resolution in images with contrast dependent on optical thickness. We illuminate a sample in a total internal reflection geometry, with a photoactivated spatial modulator in the near field, which allows optical thickness images to be computationally reconstructed in a few seconds. We demonstrate our approach at 140 GHz (wavelength 2.15 mm), where images are normally severely limited in spatial resolution, and demonstrate mapping of optical thickness variation in inhomogeneous biological tissues.

## 1. INTRODUCTION

Long-wavelength measurements such as terahertz (THz) time-domain spectroscopy are often used as a route to film thickness determination of visibly opaque materials, either using time-of-flight approaches [1,2] or through spectral analysis [3,4]. These techniques can achieve optical thickness measurements of exceptionally high accuracy, sometimes approaching micrometer scale [2,3]. However, to achieve good sensitivity to optical thickness conventionally requires illumination with near-collimated beams (i.e., only weakly focused beams with a narrow angular spectrum). This requirement limits the lateral spatial resolution of these methods, as high thickness sensitivity is not compatible with the strong focusing usually necessary to achieve high lateral resolution. This trade-off is also inherent in total internal reflection (TIR) imaging techniques that have been demonstrated to date [5,6]. The compromise between optical thickness sensitivity and lateral spatial resolution means that time-domain techniques have been most successfully employed to investigate homogeneous samples such as polymer films [7] or crystalline pallets [8].

Malleable and inhomogeneous materials, such as biological tissues, are particularly difficult to characterize by conventional means [9]. Mechanical measurements of thickness are unreliable when the sample can be compressed and time consuming if a map of varying thickness is required. Fully characterizing a sample made of opaque layers of different properties and thicknesses poses an even greater challenge. Often, cross sections of such samples are taken and studied by eye. However, this is destructive, and it does not give the full three-dimensional picture of an inhomogeneous

sample. Imaging in the THz and millimeter (mm)-wave bands offers a promising alternative for imaging the structure of inhomogeneous, and particularly biological, materials, where water absorption leads to a natural contrast mechanism [10]. In addition, THz radiation is nonionizing and hence is of particular interest for medical imaging. Recent examples of biological and medical THz imaging include the study of cartilage from the knee [11], observation of the healing process of scar tissue [12], measuring the hydration of corneas [13], and imaging water-dense cancers in breast tissue [14–16]. However, due to the low resolution associated with diffraction-limited imaging in these bands, the inherent sample inhomogeneity on subwavelength scales is a major challenge when imaging biological tissues [9]. To overcome this limitation, THz images of subwavelength surface features have been captured using near-field scanning techniques. However, weak signals typically emanating from scanning probe tips, which are sub-diffraction limited in scale, coupled with noisy detectors, result in lengthy measurement times [17–19]. Moreover, the sensitivity of detectors in the THz and mm-wave spectral bands is poor, as the low energies carried by photons make their control and detection extremely demanding. The most sensitive detectors require deep cryogenic cooling, which is problematic for the development of cameras consisting of multisensor arrays, as the individual signals from thousands of detectors must be acquired per frame.

Emerging computational imaging techniques offer a potential way forward by redefining our understanding of how images can be recorded. Such systems do not form an image directly but offload

aspects of the image formation process to a computer. "Single-pixel" computational imaging systems circumvent the need for detector arrays and boost the magnitude of near-field measurements by recording signals from many locations at once. These systems encode spatial information in the temporal dimension, enabling operation at wavelengths where multipixel sensors are challenging to fabricate, prohibitively expensive, or simply do not exist [20]. Images are reconstructed from measurements using a single-element detector, which itself records only the total incident intensity, in conjunction with a spatial light modulator (SLM). The SLM spatially modulates (i.e., varies) the intensity of light, and so enables sequential illumination of the target object with a series of patterned light fields, each of which probes a different subset of the spatial information in the scene. Recently there have been several demonstrations of deeply subwavelength single-pixel transmission imaging at THz frequencies [21–24].

In this work we demonstrate a new form of mm-wave computational imaging that enables the determination of overlayer optical thickness with significantly subwavelength precision, while also retaining subwavelength lateral resolution. We refer to our approach as a type of TIR imaging: in the absence of sample-induced loss we anticipate perfect reflection of the illuminating beam, while lossy samples reduce reflection in a spatially varying way, producing sample-dependent image contrast. Using mm-wave radiation in a TIR geometry, rather than optical frequencies as previously studied [25], means the evanescent fields can probe millimetric distances into samples—distances relevant, for example, to the determination of the thickness of structural tissue changes found in cancerous samples [26], or the study of the layered structure of the skin [27]. Our imaging approach is based upon a bespoke optically addressed mm-wave spatial modulator, integrated with a dove prism in a TIR geometry. This allows dynamic patterning of the evanescent mm-wave field probing the underside of potentially nontransmissive objects [28], granting access to a range of new types of samples, including biological tissues. This approach can capture images with subwavelength resolution for any sub-IR frequency, with an upper frequency determined by the plasma frequency of the modulator ($\sim 1 \times 10^{12}$ Hz). We show that the near-field placement of the modulator decouples the thickness sensitivity from lateral resolution, subverting the trade-off that normally limits far-field imaging approaches. As a result, and in contrast to previous single-pixel THz imaging systems, which typically produce an absorption image of a thin sample in transmission mode, our TIR geometry gives access to a richer vein of information about the sample: the reflected signal is highly sensitive to both material properties and sample thickness. To the best of our knowledge, this is the first time a near-field imaging approach has been combined with TIR, yielding the best of both worlds: the high lateral resolution of near-field imaging with the good thickness sensitivity of a TIR geometry.

Critical to the performance of our imaging system is the mm-wave spatial modulator, and we describe in detail how this has been tuned for use at mm wavelengths. This optimization balances the resolution, frame rate, and contrast of the modulator. Due to the TIR geometry, the resulting modulator is highly efficient, circumventing the requirement for high-intensity femtosecond-pulse optical pump beams [29,30], vastly simplifying the experimental setup in comparison with earlier work [31–33], removing unwanted heating of sensitive samples, and reducing optical noise. We show that our TIR-based imaging system offers a new way

forward to simultaneously image and measure the thickness of biological samples. To interpret our images throughout our study, we compare them with a transfer-matrix-based model, describing expected levels of reflection as a function of frequency, incident angle, and material parameters of the sample. We investigate the effect of the sample characteristics on image formation and experimentally show that the measured signal encodes information about both the material and the film thickness. In our proof-of-principle experiments, we show that TIR mm-wave images reveal regions of fat and protein in porcine tissue samples, highlighting the system as a good candidate for imaging water-dense samples such as cancer tumors. We also demonstrate that it is possible to detect objects embedded within a thick, optically opaque material by imaging a metal target on the far side of a fatty layer of tissue. While at present we have implemented this technique for mm-wave imaging, the principles described here could be broadly applied from gigahertz (GHz) through to THz frequencies.

## 2. DESIGNING A MM-WAVE TIR IMAGING SYSTEM

Our TIR imaging system is based on all-optical modulation (known as photomodulation), where a visible or near-IR light source is used to change the transparency of a photoactive material to low-frequency radiation. This approach is often chosen because it is relatively simple to implement, can be very fast, and can operate over a broad range of mm-wave and THz frequencies [34,35].

Figure 1(a) shows a schematic of our TIR imaging system. An IMPact ionization Avalanche Transit-Time (IMPATT) diode source (*TeraSense*, power 30 mW) produces a linearly polarized continuous wave with a frequency of 140 GHz $\pm$ 1 MHz (a wavelength of around 2.15 mm). The polarization can be switched between TE and TM by rotating both the source and detector by 90°. This passes through a dove prism made of a polymer, polymethylpentene (TPX) [36], which is transparent to both optical and GHz/THz radiation, with a refractive index of 1.58 and low loss (a tangent of $8 \times 10^{-4}$) at 140 GHz. The mm-wave spatial modulator is formed from a 390 µm thick photoactive silicon wafer placed on top of the prism, with a thin layer of immersion oil (refractive index of 1.513) between the wafer and prism to prevent air gaps. The sample is then placed on top of the silicon wafer; its proximity to the mm-wave modulator means we can pattern the mm wave on a subwavelength scale, as the fields at the surface of the silicon do not diffract. The specular mm-wave component that is totally internally reflected at the silicon–air interface is detected in the far field by a detector (Fast Detector from *TeraSense*, response time of 1 µs, typical responsivity of 10 V/W, and frequency of 140 GHz).

Before photoactivation, the silicon wafer is largely transparent to mm-wave radiation. When mm waves are incident at an angle greater than the critical angle, they are totally internally reflected from the silicon–air interface. Upon illumination of the silicon wafer with visible light, electron–hole pair photoexcitation increases the mm-wave absorption and so reduces mm-wave reflection (note that the effect of photoexcitation on the reflected signal becomes more complicated when a sample is present as explained in Section 3). Therefore, by projecting optical binary intensity patterns at normal incidence onto the silicon wafer using light from a LED pump beam (*Thorlabs SOLIS*, wavelength
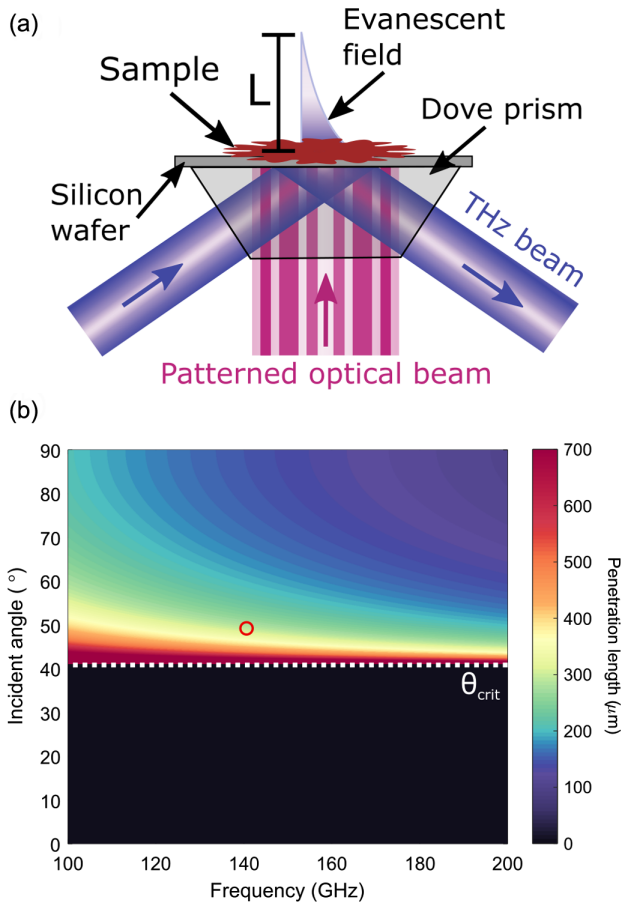
**Fig. 1.** Mm-wave imaging system. (a) Schematic showing mm-wave modulator using TIR. (b) Calculated penetration length of evanescent fields L at the silicon–air interface for a range of frequencies and angles of incidence. The 390 µm thick silicon wafer has a permittivity of $11.7 + 0.003i$, and the prism medium has a permittivity of 2.49. The white dashed line shows the critical angle, below which there are no evanescent fields, and the red circle denotes the selected experimental parameters.

$623 \pm 5$ nm, power 4.7 W) patterned with a digital micromirror device (DMD, *Vialux*), we are able to spatially control which areas of the modulator are more reflective to mm-wave radiation. In this way, the pattern in the optical pump beam is dynamically imprinted onto the mm-wave field bathing the sample, enabling single-pixel imaging to be performed. The projected optical binary patterns are drawn from the Hadamard basis. This basis yields reconstructed images with significantly higher signal-to-noise ratio (SNR) compared to simple raster scanning of a transparent (or absorbing) window, and the SNR is uniformly distributed over the reconstructed image as the set is orthogonal [37,38]. Detail of the image reconstruction can be found in Section 3.A of Supplement 1. Our data acquisition rate is nominally 2 kHz, limited by the lifetime of the charge carriers in the silicon wafer. For $64 \times 64 = 4096$ pixels, we obtain images with sufficient signal to observe features in the samples in around 4 s. To allow for low noise image analysis, the images presented below have been averaged for several minutes (see Section 3.C of Supplement 1 for a full analysis), which equates to 1 min 22 s of exposure when omitting programming wait times.

The penetration length of the evanescent field in air L [Eq. (S1) in Supplement 1] depends on both the incident angle of the mm-wave beam and its frequency as shown in Fig. 1(b). L is maximized

for low frequencies (i.e., longer wavelengths) and angles very close to the critical angle (white dotted line). These dependencies allow L to be tuned to match the sample characteristics. In this work we elected to image at a frequency of 140 GHz and incident angle of 49° [denoted by the red circle in Fig. 1(b)], giving a penetration depth in air of ~300 µm.

## 3. RESPONSIVITY TO SAMPLE THICKNESS

When a layer of material is placed on top of the silicon wafer, the intensity of the mm-wave beam reflected back into the detector depends upon both the complex refractive index and thickness of the layer. If the refractive index of the material is less than that of the prism, one expects evanescent fields at the silicon–sample boundary that are sensitive to the properties of the sample [28]. If the sample has an index higher than the prism, one breaks the TIR condition at the silicon–sample interface, allowing a propagating wave to interrogate the sample layer.

To study these effects, we image a step in a polymer sample of known height and permittivity ($3.5 + 0.53i$), and we compare the image to the prediction from a transfer matrix calculation as described in reference [39]. The sample under investigation is created by layering cellulose from tape to create films of different thicknesses. Reconstructed images are spatial maps of $\delta r(x, y) = \delta r_0(x, y)/\text{MD}(x, y)$, which is the difference in reflected signal at each spatial location $(x, y)$, as the mm-wave modulator is switched from its Off (dark) to On (i.e., photoactivated) state with a sample $\delta r_0(x, y)$ present, normalized to the modulation depth MD, which is the same measurement with no sample present. This normalization removes artefacts that arise from inhomogeneities in the mm-wave spot. Figure 2(a) shows the predicted level of $\delta r$ as a function of incident angle and sample thicknesses. Circles (1) and (2) indicate the expected signals at thicknesses of $350 \pm 10$ µm and $570 \pm 10$ µm. Figure 2(b) shows experimentally obtained visible (left panel) and mm-wave (right panel) images of the polymer step.

One intriguing feature of Fig. 2 is that the sign of $\delta r$ changes as a function of thickness. $\delta r > 0$ indicates a decrease in reflection of mm-wave radiation on photoexcitation of the silicon wafer, while $\delta r < 0$ indicates an increase. $\delta r < 0$ is somewhat unexpected: Why would an introduction of absorption into the silicon layer lead to an *increase* in the level of reflected radiation? This surprising effect arises due to an optimal matching condition between the absorption and radiative loss channels of the system, which defines critical coupling conditions [40]. This is similar to an effect observed for plasmonic cavities [41,42] and arises here due to a Fabry–Pérot resonance present in the sample itself. It is clear that the change in sign of $\delta r$ is both predicted in our wave modeling [Fig. 2(a)] and observed in experiment [Fig. 2(b)]. However, the negative signals measured in experiment have a larger magnitude than those predicted from our modeling; we suspect this arises due to small air gaps in between cellulose layers changing the matching condition. Nevertheless, as demonstrated, an image contrast ($\delta r$) which *varies in sign* upon a change in sample thickness of an order of magnitude smaller than the wavelength, has significant measurement potential, especially for challenging samples made from malleable and soft materials. Furthermore, we show in Section 4.7 of Supplement 1 that if we could take several images at different angles of incidence, it is possible to simultaneously extract both the thickness and complex refractive index of a sample using our technique. This
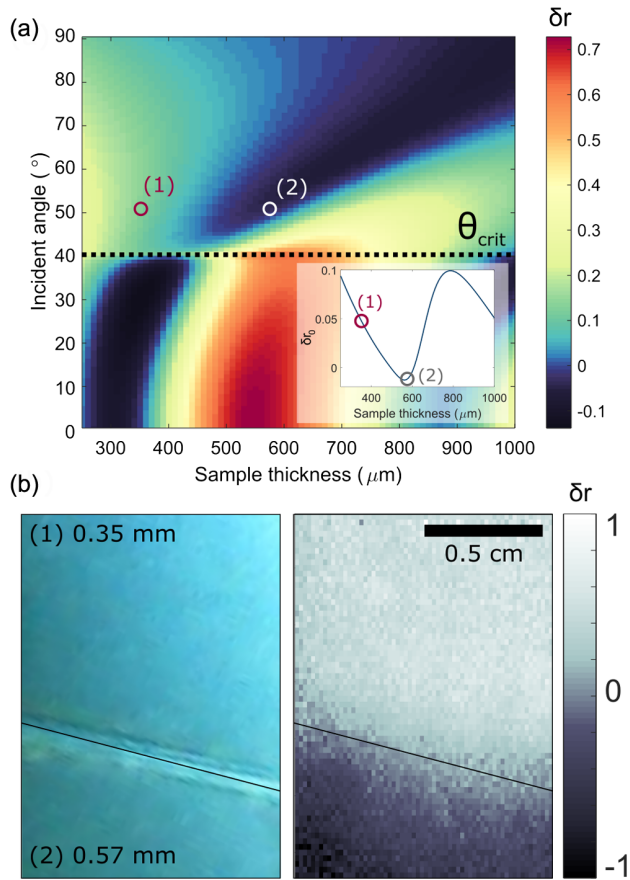
**Fig. 2.** Determining the thickness of a sample. (a) Calculated $\delta r$ when a sample of permittivity $3.5 + 0.53i$ is present on top of the silicon wafer, as a function of sample thickness and incident angle of the mm-wave beam. The inset shows the unnormalized $\delta r_0$ at 50° incidence. Results are calculated at 140 GHz frequency and TE polarization, and an incident photoexcitation wavelength of 623 nm and power of $220\,\mathrm{Wm^{-2}}$ when illuminated, and $0\,\mathrm{Wm^{-2}}$ when dark. The silicon wafer has a thickness of 390 µm and a charge carrier lifetime of 75 µs. The critical angle is marked by the dotted black line. The red and white (inset: gray) circles (1) and (2) denote the parameters corresponding to the image in (b). (b) Optical (left) and mm-wave (right) images of a polymer sample with regions of two different thicknesses, with the same measurement parameters as the simulation.

---

is only possible due to the well-defined incident angle in our measurement approach, and is not usually possible in high-resolution imaging, as the angular distribution required for a focused spot is incompatible with well-defined angle dependencies. This issue is also often faced by, e.g., time-of-flight measurements, where the delay of pulses depends on the optical path length, and it is not possible to separate this into contributions from the sample thickness and refractive index.

## 4. IMAGING BIOLOGICAL TISSUE

We now demonstrate imaging of inhomogeneous biological tissues using our mm-wave TIR imaging system. The sample is a $750 \pm 250$ µm thick piece of sliced porcine tissue, which exhibits strong spatial variation in properties, varying from fatty to protein-rich regions. While one can expect a high degree of variation in the complex permittivities of biological tissues (see Section 4.6 of Supplement 1) [15,26,43,44], for now in our model we assume
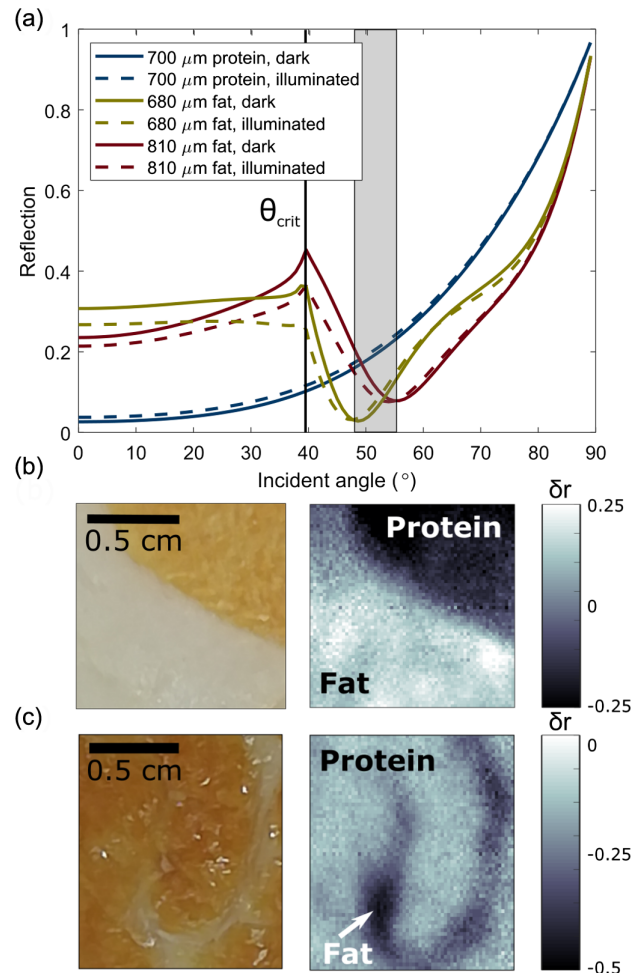


**Fig. 3.** Imaging biological tissue. (a) Calculated reflection of a TE-polarized mm wave at 140 GHz when various biological tissues are placed on top of the silicon wafer, when the silicon is dark (solid lines) or illuminated (dashed lines) with a photoexcitation beam of $220\,\mathrm{Wm^{-2}}$ at 623 nm wavelength. The silicon wafer has a thickness of 390 µm and a charge carrier lifetime of 75 µs. The critical angle ($\theta_{\mathrm{crit}}$, black vertical line) and the range of angles where the $\delta r$ is of opposite sign for the two different thicknesses of fat (gray shaded area) are marked on the plot. (b) and (c) Images of porcine tissue samples at visible (left) and 140 GHz (right) frequencies: (b) shows a large fatty region well separated from the protein, and (c) shows thin filaments of fat embedded in protein, while the regions of fat and protein are clearly distinguishable in both. The $64 \times 64$ pixel mm-wave images are an average of 100 images taken with TE polarization, where each took 4.1 s to collect (images collected over shorter times can be found in Section 3.3 of Supplement 1).

---

protein-rich and fatty tissues are described by $\epsilon_{\mathrm{fat}} = 2.89 + 0.64i$ and $\epsilon_{\mathrm{protein}} = 8.63 + 11.20i$, taken from Reference [45]. Using these values, Fig. 3(a) shows modeling of reflected mm-wave signal when a layer of fat or protein is placed on top of the wafer, as a function of incident angle, for both photoactivated ($220\,\mathrm{Wm^{-2}}$) and dark silicon. We show modeling results for three different thicknesses of material within the experimentally measured range.

Our model indicates that materials with high losses, such as protein, do not exhibit strong variation in $\delta r$ as sample thickness changes, due to the strong absorption of the mm-wave beam. We show the dependency of reflection on incident angle for a single thickness of protein tissue (700 µm, blue plot) in Fig. 3(a). We also

see that the difference in predictions for illuminated and nonilluminated modulators is very small (i.e., $\delta r$ is expected to be small) for protein tissue. There are two factors that determine this: first the absorption of the mm wave is higher in protein than in fat, due to its higher water content; second, the real part of the refractive index of protein is close to that of silicon, and therefore a significant drop in the reflection is expected in this case. Fatty tissue, on the other hand, has a much lower water content, and hence absorption is lower. We predict fatty tissue will exhibit a strong variation of $\delta r$ on changing sample thickness. This is shown in the red and yellow plots in Fig. 3(a), which show reflection as a function of incident angle for two thicknesses (680 μm, yellow plot and 810 μm, red plot). Here we see that $\delta r$, the difference between dashed and solid lines, is expected to change sign when passing through the minimum in reflection at around 50° (60°) for a thickness of 680 μm (810 μm). We therefore see a range of angles, marked by the gray region, where we expect the signal to be completely opposite in sign for a thickness difference of just 130 μm (i.e., just 5% of the mm-wave wavelength).

In Figs. 3(b) and 3(c) we present mm-wave images of two different samples of porcine tissue: (b) one with a large region of fat well separated from the protein-rich region and (c) one with filaments of fat on the scale of the imaging wavelength running through. In both images, the regions of fat and protein are clearly distinguishable, as seen by comparison to the optical images on the left. As predicted, $\delta r$ is close to zero within regions of protein in both Figs. 3(b) and 3(c). Approximate measurements using a set of vernier calipers gave the thickness of fatty regions in Fig. 3(b) to be 810 ± 200 μm, while the thickness of the fat in Fig. 3(c) was estimated to be 680 ± 150 μm. As predicted by our model, the measured $\delta r$ of fatty tissue regions in each image have opposite signs. We present further simulations in Section 4.5 of Supplement 1 that illustrate this sensitivity to permittivity and sample thickness.

The low absorption of fat also allows us to image objects behind layers of fatty tissue. This is shown experimentally in Section 4.8 of Supplement 1 and demonstrates imaging through visibly opaque fatty tissues to yield information on the structure of a sample that would not otherwise be known.

## 5. EXPLORING PHYSICAL LIMITATIONS OF THE SYSTEM

There are several interrelated factors that determine the performance of our TIR computational imaging system. Conventional diffraction-limited imaging systems can reach resolutions of $\sim\lambda/2\mathrm{NA}$, where NA is the numerical aperture defined by the distribution of incident rays. To achieve high depth sensitivity, one requires illumination with near-collimated mm waves: our system has a mm-wave NA = 0.06, similar to NAs used in both time-of-flight systems [1,2] and previous TIR imaging systems [5,6]. An NA = 0.06 corresponds to an expected diffraction-limited resolution $\sim$1.8 cm for 140 GHz—this demonstrates the trade-off between lateral and depth resolution normally inherent to both time-of-flight and TIR approaches. However, in our design, the in-plane lateral resolution of images is determined by the local modulation of the incident mm wave by our photomodulator. As shown in Supplement 1, Section 4.3, due to the low NA of our detector, our signals are dominated by the specular reflection from the sample, which maintains the low angular dispersion of the measurement. Yet the specular reflection is still affected by

local photomodulation, as can be seen by the small spatial features evident in Fig. 3(c) (the narrow vein of fat, highlighted by the white arrow) and Section 4.2 in Supplement 1. In this case, the image resolution will be determined by the optical pump beam, and subsequent charge carrier diffusion within the silicon wafer (i.e., how far the charge carriers drift, thus blurring the optical pump pattern), rather than the wavelength of the mm-wave beam, meaning sub-diffraction-limited imaging is possible. Figure 4(a) shows how the diffusion of charge carriers in the silicon depends on their effective lifetime. Reconstructed images inherit the same level of blurring that the patterning of the mm-wave field has undergone, due to drift of charge carriers. In this case the point spread function of the system is governed by the drift-induced long-range correlations in the mm-wave field patterns used to probe the object [46]. The lifetime of the wafer chosen for our experiments is 75 μs (float zone silicon bought from Siltronix, dark resistivity = 5 kΩ,
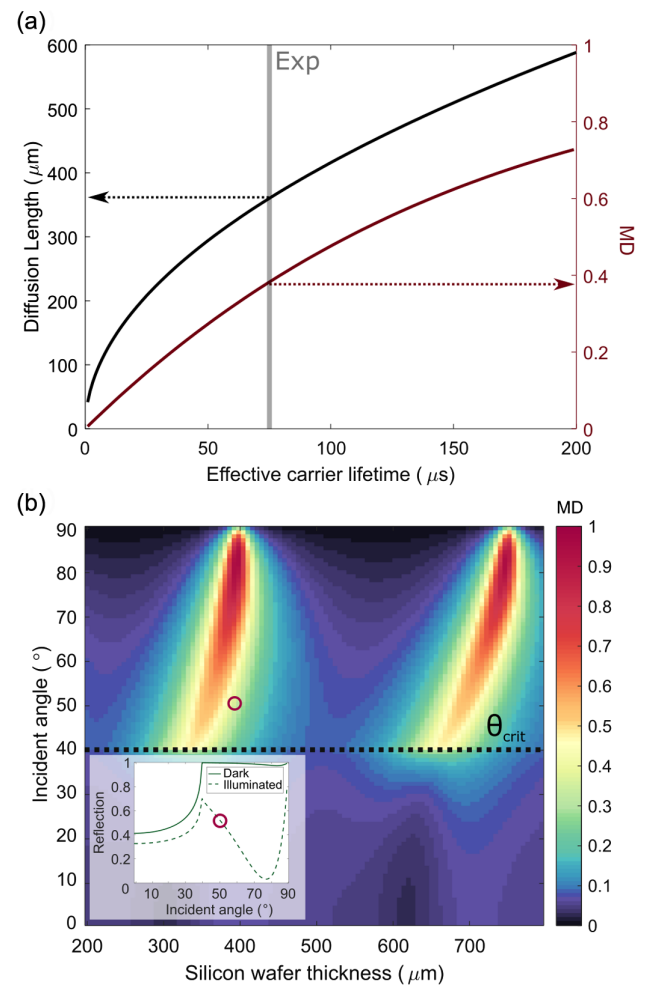


**Fig. 4.** Investigating design parameters. (a) Calculated diffusion length of carriers (left, black axis) and modulation depth (right, red axis) as a function of effective charge carrier lifetime for a mm-wave beam incident at 50° through the prism material onto a 390 μm thick wafer. The gray line shows the lifetime of the wafer used in experiment. (b) TE-polarized modulation depth of a mm-wave signal as function of angle of incidence in the prism material and silicon wafer thickness, assuming a charge carrier lifetime of 75 μs. Inset shows the reflection for dark and illuminated states for a 390 μm thick wafer. All results are calculated at 140 GHz mm-wave frequency, and an incident photoexcitation wavelength of 623 nm and power of 220 Wm$^{-2}$ when illuminated, and 0 Wm$^{-2}$ when dark. The red circles show the experimental parameters.

thickness = 390 μm, 120 nm of $SiO_2$ passivation; see Section 2.4 of Supplement 1 for more information). A lifetime of 75 μs leads to a diffusion length of 350 μm, and a lateral resolution of twice this value i.e., 700 μm, which agrees with the resolutions observed in our images.

There is also scope to achieve lateral resolutions far below our experimental limit by reducing the effective carrier lifetime of the modulator [39]. However, Fig. 4(a) also shows that, for a given optical pump power, decreasing the carrier lifetime simultaneously decreases the reflection modulation depth $MD = R_{dark} - R_{illum}$, which depends on the reflected intensity of the mm wave when the silicon is dark ($R_{dark}$) and illuminated ($R_{illum}$). Ultimately, MD is a function of carrier lifetime, as one can achieve a higher photoconductivity for longer lifetimes (see Section 5). For our experiment, a lifetime of 75 μs provided a reasonable trade-off between resolution and MD, while higher MD comes at a cost of lower imaging resolution. Conversely, for applications where long imaging times and averaging are possible, one could trade SNR in return for significantly higher imaging resolution.

There are other parameters we can tune to ensure that MD is maximized without compromising on the speed and resolution of imaging—namely, the incident angle, wafer thickness, and frequency. In Fig. 4(b) we show the numerically calculated MD as a function of incident angle and silicon wafer thickness, on a TPX–silicon–air stack (calculated here for TE polarization and 140 GHz with an excitation intensity of 220 $Wm^{-2}$ and excitation wavelength of 623 nm for a silicon wafer with effective charge carrier lifetime $\tau_{eff} = 75$ μs). The inset shows the reflected mm-wave intensity (for dark and illuminated states) for a 390 μm thick wafer. For a stack of TPX–silicon–air we predict the onset of TIR for a critical angle of $\theta_{crit} = 39.3°$. For angles beyond $\theta_{crit}$, the modulation depth is around an order of magnitude larger than that achieved at normal incidence. The incident angle that provides the largest modulation depth is near grazing incidence. However, as discussed earlier, angles closer to the critical angle give evanescent fields, which penetrate further into low-index samples [see Fig. 1(b)], so we opt for an angle of 49°, marked by the red circle, where the penetration length of the field is around 300 μm in air.

It is also clear from Fig. 4(b) that the modulation depth is dependent on the thickness of the silicon wafer. This arises due to a cavity resonance in the wafer, as reported in [39], which gives an increased modulation depth when the wafer thickness is equal to a half-integer multiple of the wavelength in silicon. For a mm-wave frequency of 140 GHz, we choose a wafer that is 390 μm thick; close to the resonance but limited by commercially available silicon wafers.

## 6. CONCLUSIONS

In conclusion, we have demonstrated the first computational near-field imaging system in a TIR geometry. This unique combination allows images of sample structure to be reconstructed with subwavelength lateral resolution and subwavelength optical depth sensitivity, which is not possible with other techniques [3,5,30]. In comparison with previously demonstrated THz and mm-wave computational imaging systems [4,5,31], our design exhibits a high pixels-per-second rate of several kilohertz (kHz), which gives a resolution-dependent frame rate of a few seconds. Our TIR system is also cheaper and more compact than those of previous works, as it circumvents the need for femtosecond-pulsed lasers.

The penetration depth of the illuminating field is dependent on both incident angle and mm-wave frequency, pointing to an intriguing avenue for future development of the system: by capturing several images at a range of incident angles and frequencies, there is potential to decouple material parameters from layer thickness and so independently recover these sample properties simultaneously. Section 4.7 of Supplement 1 details modeling that demonstrates this principle for some simple cases. In the future it may be possible to extend this approach to recover TIR-based tomographic images of more complex samples that exhibit strong inhomogeneity in all three dimensions. Our future work will explore the feasibility of 3D image reconstruction from these measurements, supported by varying degrees of prior information about the sample. Together, we believe these features point towards many potential applications of mm-wave computational TIR imaging for interrogation of the structure of optically opaque samples in, for example, the medical, art conservation, and food industries.

See Supplement 1 for supporting content.

†These authors contributed equally to this work.

## REFERENCES

1. H. Zhong, J. Xu, X. Xie, T. Yuan, R. Reightler, E. Madaras, and X. C. Zhang, "Nondestructive defect identification with terahertz time-of-flight tomography," IEEE Sens. J. **5**, 203–207 (2005).
2. E. Abraham, A. Younus, J. C. Delagnes, and P. Mounaix, "Non-invasive investigation of art paintings by terahertz imaging," Appl. Phys. A **100**, 585–590 (2010).
3. J. L. Johnson, T. D. Dorney, and D. M. Mittleman, "Enhanced depth resolution in terahertz imaging using phase-shift interferometry," Appl. Phys. Lett. **78**, 835–837 (2001).
4. T. Nagatsuma, T. Ikeo, and H. Nishii, "Terahertz imaging based on optical coherence tomography," in ICECom–Conf. Proceedings: 21st Int. Conf. on Appl. Electromagn. Commun. (2013), Vol. **2**, pp. 64–69.
5. A. Wojdyla and G. Gallot, "Attenuated internal reflection terahertz imaging," Opt. Lett. **38**, 112–114 (2013).
6. M. Grognot and G. Gallot, "Quantitative measurement of permeabilization of living cells by terahertz attenuated total reflection," Appl. Phys. Lett. **107**, 103702 (2015).
7. L. Chen, Y. Ge, X. Zang, J. Xie, L. Ding, A. V. Balakin, A. P. Shkurinov, and Y. Zhu, "Tunable phase transition via radiative loss controlling in a terahertz attenuated total reflection-based metasurface," IEEE Trans. Terahertz Sci. Technol. **9**, 643–650 (2019).
8. D. G. A. Ibrahim, S. K. Khalil, H. H. Sherif, and M. M. Eloker, "Multilayer film thickness measurement using ultrafast terahertz pulsed imaging," J. Phys. Commun. **3**, 035013 (2019).

9. T. C. Bowman, M. El-Shenawee, and L. K. Campbell, "Terahertz imaging of excised breast tumor tissue on paraffin sections," IEEE Trans. Anntenas Propag. **63**, 2088–2097 (2015).

10. Y. He, K. Liu, C. Au, Q. Sun, E. P. Parrott, and E. Pickwell-MacPherson, "Determination of terahertz permittivity of dehydrated biological samples," Phys. Med. Biol. **62**, 8882–8893 (2017).

11. R. I. Stantchev, J. C. Mansfield, R. S. Edginton, P. Hobson, F. Palombo, and E. Hendry, "Subwavelength hyperspectral THz studies of articular cartilage," Sci. Rep. **8**, 6924 (2018).

12. S. Fan, B. S. Ung, E. P. Parrott, V. P. Wallace, and E. Pickwell-MacPherson, "In vivo terahertz reflection imaging of human scars during and after the healing process," J. Biophoton. **10**, 1143–1151 (2017).

13. Z. D. Taylor, J. Garritano, S. Sung, N. Bajwa, D. B. Bennet, B. Nowroozi, P. Tewari, J. W. Sayre, J.-P. Hubschman, S. X. Deng, E. R. Brown, and W. S. Grundfest, "THz and mm-wave sensing of corneal tissue water content: in vivo sensing and imaging results," IEEE Trans. Terahertz Sci. Technol. **5**, 184–196 (2015).

14. C. Yu, S. Fan, Y. Sun, and E. Pickwell-MacPherson, "The potential of terahertz imaging for cancer diagnosis: a review of investigations to date," Quant. Imaging Med. Surg. **2**, 33–45 (2012).

15. P. C. Ashworth, E. Pickwell-MacPherson, E. Provenzano, S. E. Pinder, A. D. Purushotham, M. Pepper, and V. P. Wallace, "Terahertz pulsed spectroscopy of freshly excised human breast cancer," Opt. Express **17**, 12444–12454 (2009).

16. A. J. Fitzgerald, E. Pickwell-MacPherson, and V. P. Wallace, "Use of finite difference time domain simulations and debye theory for modelling the terahertz reflection response of normal and tumour breast tissue," PLoS ONE **9**, e99291 (2014).

17. J. Zhao, W. Chu, L. Guo, Z. Wang, J. Yang, W. Liu, Y. Cheng, and Z. Xu, "Terahertz imaging with sub-wavelength resolution by femtosecond laser filament in air," Sci. Rep. **4**, 3880 (2014).

18. M. Eisele, T. L. Cocker, M. A. Huber, M. Plankl, L. Viti, D. Ercolani, L. Sorba, M. S. Vitiello, and R. Huber, "Ultrafast multi-terahertz nanospectroscopy with sub-cycle temporal resolution," Nat. Photonics **8**, 841–845 (2014).

19. F. Blanchard, A. Doi, T. Tanaka, H. Hirori, H. Tanaka, and Y. Kadoya, "Real-time terahertz near-field microscope," Opt. Express **19**, 3523–3525 (2011).

20. E. Hack, L. Valzania, G. Gäumann, M. Shalaby, C. P. Hauri, and P. Zolliker, "Comparison of thermal detector arrays for off-axis THz holography and real-time THz imaging," Sensors (Switzerland) **16**, 221 (2016).

21. W. L. Chan, J. Deibel, and D. M. Mittleman, "Imaging with terahertz radiation," Rep. Prog. Phys. **70**, 1325–1379 (2007).

22. D. Shrekenhamer, C. M. Watts, and W. J. Padilla, "Terahertz single pixel imaging with an optically controlled dynamic spatial light modulator," Opt. Express **21**, 12507–12518 (2013).

23. S. A. N. Saqueb and K. Sertel, "Phase-sensitive THz imaging using single-pixel intensity-only measurements," in *IEEE International Symposium on Antennas and Propagation (APSURSI)* (2016), Vol. **6**, pp. 1065–1066.

24. S. M. Hornett, R. I. Stantchev, M. Z. Vardaki, C. Beckerleg, and E. Hendry, "Subwavelength terahertz imaging of graphene photoconductivity," Nano Lett. **16**, 7019–7024 (2016).

25. D. Axelrod, "Total internal reflection fluorescence microscopy," Encycl. Cell Biol. **2**, 62–69 (2016).

26. T. Bowman, M. El-Shenawee, and L. K. Campbell, "Terahertz transmission vs reflection imaging and model-based characterization for excised breast carcinomas," Biomed. Opt. Express **7**, 3756–3783 (2016).

27. E. Pickwell, B. E. Cole, A. J. Fitzgerald, M. Pepper, and V. P. Wallace, "In vivo study of human skin using pulsed terahertz radiation," Phys. Med. Biol. **49**, 1595–1607 (2004).

28. M. L. Martin-Fernandez, C. J. Tynan, and S. E. D. Webb, "A 'pocket guide' to total internal reflection fluorescence," J. Microsc. **252**, 16–22 (2013).

29. X. Liu, E. P. Parrott, B. S. Ung, and E. Pickwell-MacPherson, "Exploiting total internal reflection geometry for efficient optical modulation of terahertz light," APL Photon. **1**, 076103 (2016).

30. R. I. Stantchev, X. Yu, T. Blu, and E. Pickwell-Macpherson, "Real-time terahertz imaging with a single-pixel detector," Nat. Commun. **11**, 2535 (2020).

31. R. I. Stantchev, B. Sun, S. M. Hornett, P. A. Hobson, G. M. Gibson, M. J. Padgett, and E. Hendry, "Noninvasive, near-field terahertz imaging of hidden objects using a single-pixel detector," Sci. Adv. **2**, e1600190 (2016).

32. T. Nozokido, H. Minamide, and K. Mizuno, "Modulation of submillimeter wave radiation by laser-produced free carriers in semiconductors," Electron. Commun. Jpn. **80**, 259–266 (1997).

33. T. Okada and K. Tanaka, "Photo-designed terahertz devices," Sci. Rep. **1**, 121 (2011).

34. Y. Bai, T. Bu, K. Chen, and S. Zhuang, "Review about the optical-controlled terahertz waves modulator," Appl. Spectrosc. Rev. **50**, 707–727 (2015).

35. M. Rahm, J. S. Li, and W. J. Padilla, "THz wave modulators: a brief review on different modulation techniques," J. Infrared, Millimeter, Terahertz Waves **34**, 1–27 (2013).

36. C. M. A. Inc, *TPX Datasheet* (2019).

37. N. J. Sloane and M. Harwit, "Masks for Hadamard transform optics, and weighing designs," Appl. Opt. **15**, 107–114 (1976).

38. J. A. Decker, "Hadamard-transform image scanning," Appl. Opt. **9**, 1392–1395 (1970).

39. I. R. Hooper, N. E. Grant, L. E. Barr, S. M. Hornett, J. D. Murphy, and E. Hendry, "High efficiency photomodulators for millimeter wave and THz radiation," Sci. Rep. **9**, 18304 (2019).

40. H. A. Haus, *Waves and Fields in Optoelectronics* (Prentice-Hall, 1984).

41. S. Herminghaus, M. Klopfleisch, and H. J. Schmidt, "Attenuated total reflectance as a quantum interference phenomenon," Opt. Lett. **19**, 293 (1994).

42. H. Raether, *Surface Plasmons on Smooth and Rough Surfaces and on Gratings*, 1st ed. (Springer-Verlag, 1988).

43. Y. Sun, B. M. Fischer, and E. Pickwell-MacPherson, "Effects of formalin fixing on the terahertz properties of biological tissues," J. Biomed. Opt. **14**, 064017 (2009).

44. Y. Sun, "A promising diagnostic method: terahertz pulsed imaging and spectroscopy," World J. Radiol. **3**, 55 (2011).

45. C. Gabriel and S. Gabriel, "Compilation of the dielectric properties of body tissues at RF and microwave frequencies," Tech. Rep. (1996).

46. D. B. Phillips, R. He, Q. Chen, G. M. Gibson, and M. J. Padgett, "Non-diffractive computational ghost imaging," Opt. Express **24**, 14172–14182 (2016).